nature nanotechnology

SUPPLEMENTARY INFORMATION

https://doi.org/10.1038/s41565-018-0233-9

In the format provided by the authors and unedited.

Nano-imaging of intersubband transitions in van der Waals quantum wells

Peter Schmidt[1], Fabien Vialla[1,2], Simone Latini[3,4], Mathieu Massicotte[1], Klaas-Jan Tielrooij[1], Stefan Mastel[5], Gabriele Navickaite[1], Mark Danovich[6], David A. Ruiz-Tijerina[6], Celal Yelgel[6], Vladimir Fal'ko[6], Kristian S. Thygesen[3], Rainer Hillenbrand[5,7] and Frank H. L. Koppens[1,8]*

[1]ICFO - Institut de Ciències Fotòniques, The Barcelona Institute of Science and Technology, Castelldefels (Barcelona), Spain. [2]Institut Lumière Matière UMR5306, Université Claude Bernard Lyon1 – CNRS, Villeurbanne , France. [3]Center for Atomic-scale Materials Design, Technical University of Denmark, Kongens Lyngby, Denmark. [4]Max Planck Institute for the Structure and Dynamics of Matter, Hamburg, Germany. [5]CIC nanoGUNE Consolider, Donostia-San Sebastián, Spain. [6]National Graphene Institute, University of Manchester, Manchester, UK. [7]IKERBASQUE, Basque Foundation for Science, Bilbao, Spain. [8]ICREA-Institució Catalana de Recerca i Estudis Avançats, Barcelona, Spain. *e-mail: frank.koppens@icfo.eu

I DFT calculations

In order to provide the theoretical frame work for intersubband transition in van der Waals quantum wells, we calculated band structures and intersubband transition energies, using two different density functional theory (DFT) approaches. The first approach employs the GPAW code as part of the CAMPOS software, while the second approach uses the PWSCF *ab initio* package of Quantum Espresso. Each of the two approaches is described in more detail in the following sections. Both approaches yield qualitative and quantitative similar results for the relevant values of our experiment.

I.1 DFT calculations using the GPAW code

We calculate few-layer TMD band structures and wave functions using *ab initio* density functional theory (DFT). All of the *ab initio* calculation in this work are performed with the GPAW code (*1*). The GPAW code is available as part of the CAMPOS software: `https://wiki.fysik.dtu.dk/gpaw/`. The band structures for the different flakes were calculated at the DFT level with an LDA exchange correlation functional with a plane-wave basis set. More specifically we used a cut off energy for the plane-wave basis of 500 eV and a 45x45 k-point grid. For the squared wave-function representation in the out-of-plane direction we integrated the $|\Psi(x,y,z)|^2$ along the in-plane unit cell. We stress that the reported wave functions are all-electron wave functions as they include the PAW corrections from the core electrons. As for the geometry of the MoS_2 and WSe_2 we used the following values: a_{MoS_2} = 3.184 Å and a_{WSe_2} = 3.319 Å for the lattice parameters, $d_{S\text{-}S}$ = 3.127 Å and $d_{Se\text{-}Se}$ = 3.359 Å for the chalcogen-chalcogen distance and d_{MoS_2} = 6.293 Å and d_{WSe_2} = 6.718 Å for the interlayer distances.

Figure S1 and Figure S2 show the obtained band structures for WSe_2 and MoS_2 flakes with layer numbers N = 3-6. We observe that N-layer thick flakes show N subbands in the conduction

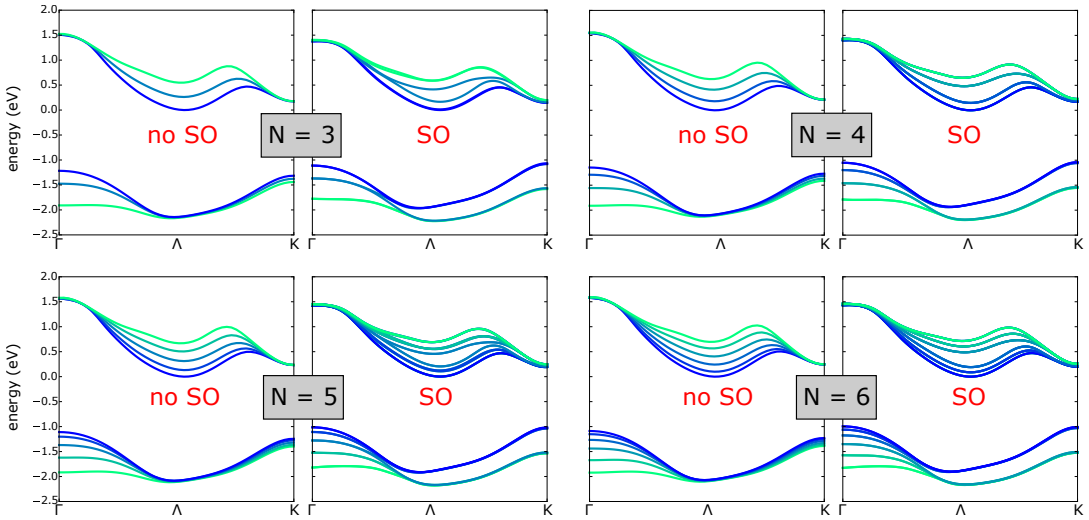

Figure S1: DFT bandstructure calculations for WSe_2 crystals with N = 3-6, with and without SO coupling. Shown are the highest valence bands and lowest conduction bands between the Γ and K point of the Brillouin zone.

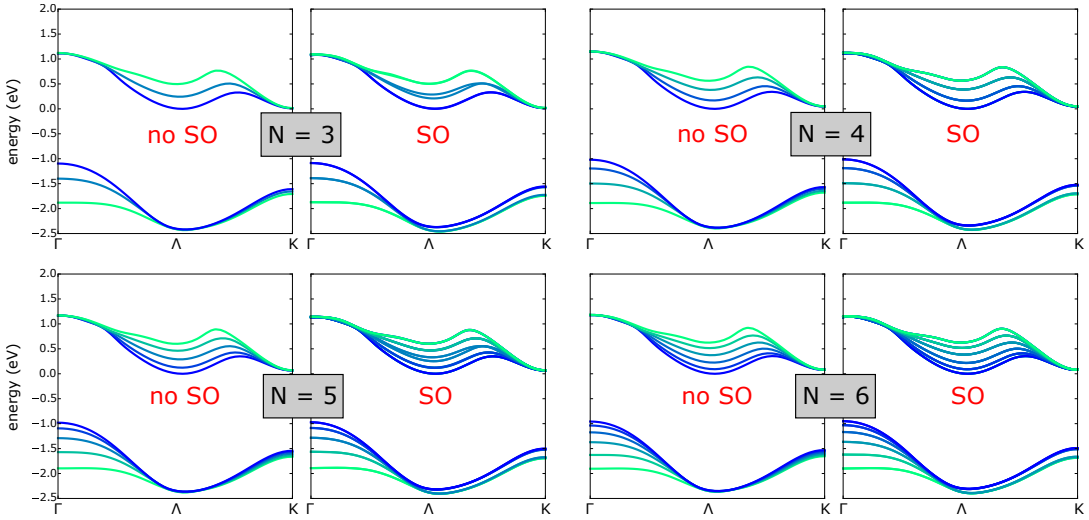

Figure S2: DFT bandstructure calculations for MoS_2 crystals with N = 3-6, with and without SO coupling. Shown are the highest valence bands and lowest conduction bands between the Γ and K point of the Brillouin zone.

and valence band (spin-orbit (SO) coupling leads to an additional splitting of the conduction bands for odd N). We see that for both, WSe_2 and MoS_2, the subband splitting mainly occurs around the conduction band minimum (Λ point) and around the valence band maximum (Γ

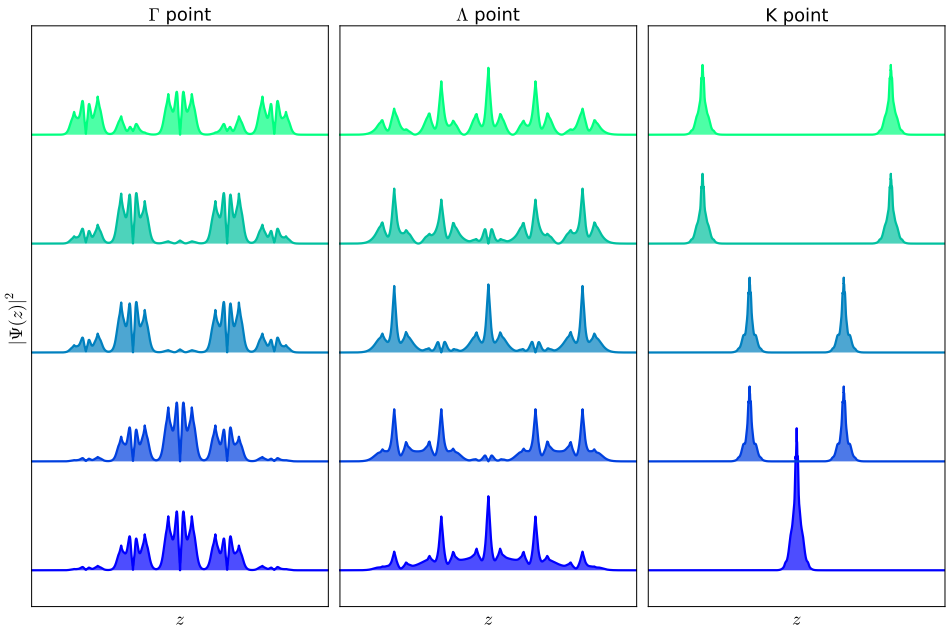

Figure S3: Out-of-plane electron wave functions for a 2H-WSe_2 crystal with $N = 5$ at the Γ, Λ, and K point of the Brillouin zone for the five lowest conduction bands.

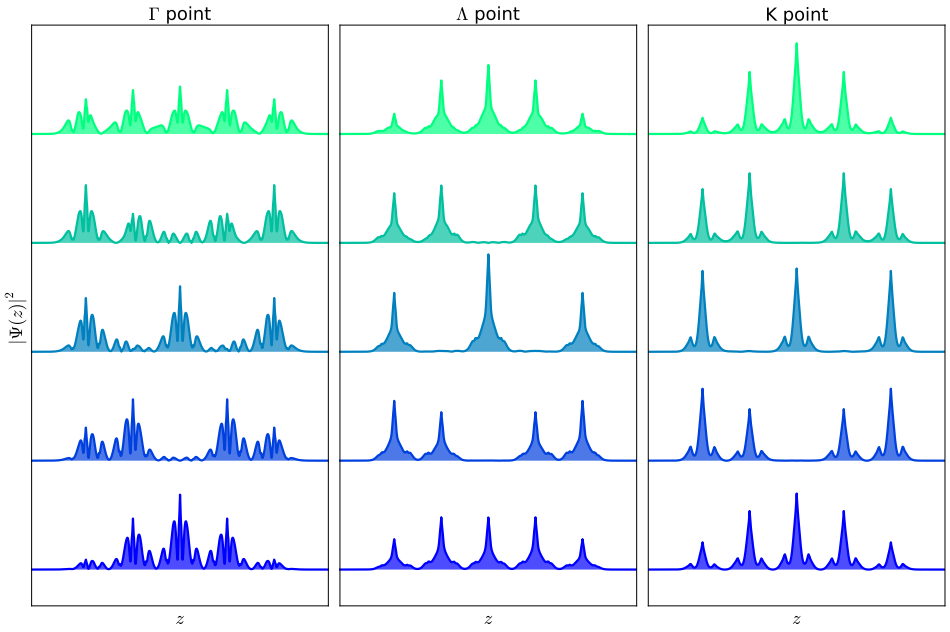

Figure S4: Out-of-plane hole wave functions for a 2H-WSe_2 crystal with $N = 5$ at the Γ, Λ, and K point of the Brillouin zone for the five highest valence bands.

point). This is due to the fact that only around these points of the Brillouin zone, the wave functions of different layers overlap so that charge carriers become mobile in the out-of-plane direction (*2*). This becomes more evident when looking at the out-of-plane wave functions at the Γ, Λ and K point of the Brillouin zone. The squared out-of-plane (in-plane integrated) wave functions $|\Psi(z)|^2$ for electrons in a 2H-WSe_2 crystal with N = 5 are shown in Figure S3. We observe that at the Λ point there is a finite probability of finding an electron between the layers. This is in stark contrast to the Γ and in particular the K point, where the electrons are completely confined within their respective layers and no coupling between the layers can be observed. This explains why the electron subband splitting only occurs around the Λ point for the electrons. A similar observation can be made for the out-of-plane wave functions of the holes, which are shown in Figure S4 for WSe_2 with N = 5. We find a very good coupling between the layers at the Γ point of the Brillouin zone, while the holes are confined within their respective layers at the Λ and K point, explaining the absence of a significant subband splitting at these points of the Brillouin zone. The same behaviour of the out-of-plane wave functions can be found for MoS_2 and different N.

In order to determine the relevant intersubband transitions we evaluate the transition matrix elements from the first to the *j*-th subband. We only consider transitions from the first subband since it is the only subband that can be populated with electrons or holes by electrostatic doping. The transition matrix element between the first and *j*-th subband is evaluated as $\langle \Psi_1 | \, \mathrm{e}^{iqz} \, | \Psi_j \rangle$ for $q \to 0$ with Ψ_j being the wavefunction of the *j*-th subband and q being the momentum in z direction. The calculated transition matrix elements are shown in Figure S5 for holes in WSe_2 and electrons in MoS_2 for N = 5 crystals. Other layer thicknesses show qualitative similar results. We see that transitions from the first to the third or fifth subband have a transition matrix element close to zero meaning that these are forbidden transitions. This observation can be explained by considering solutions to an infinite square well potential, where due to symmetry

reasons only transitions between subbands of opposite parities are allowed. For the remaining allowed transitions, the transition from the first to the second subband is about two orders of magnitude stronger than the transition from the first to the fourth subband and is therefore the only relevant transition that we consider in our experiments.

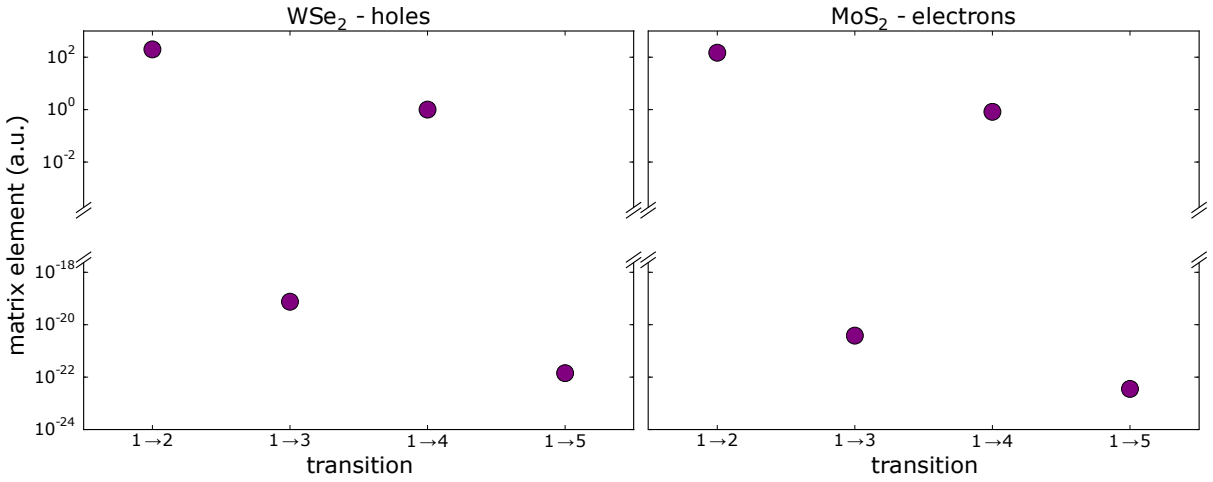

Figure S5: Transition matrix elements (defined as $\langle \Psi_1 | \, \mathrm{e}^{iqz} \, | \Psi_j \rangle$, $q \to 0$) for holes at the Γ point for a WSe_2 crystal and electrons at the Λ for a MoS_2 crystal with $N = 5$. Only transitions from the first subband are shown since it is the subband that can be populated in our experiment by using electrostatic doping.

I.2 DFT calculations using the PWSCF *ab initio* package

The band structures of few layer 2H–stacked TMDs were obtained using density function theory (DFT). The DFT calculations were performed using a plane–wave basis within the local density approximation (LDA), with the PWSCF *ab initio* package of Quantum Espresso (*3*). We considered the Perdew–Zunger exchange correlation scheme, with fully–relativistic norm–conserving pseudopotentials, including non–collinear corrections. The cutoff energy in the plane–wave expansion was set to 60 Ry, and the Brillouin zone sampling of electronic states was approximated using a Monkhorst–Pack uniform k–grid of $24 \times 24 \times 1$ for all structures.

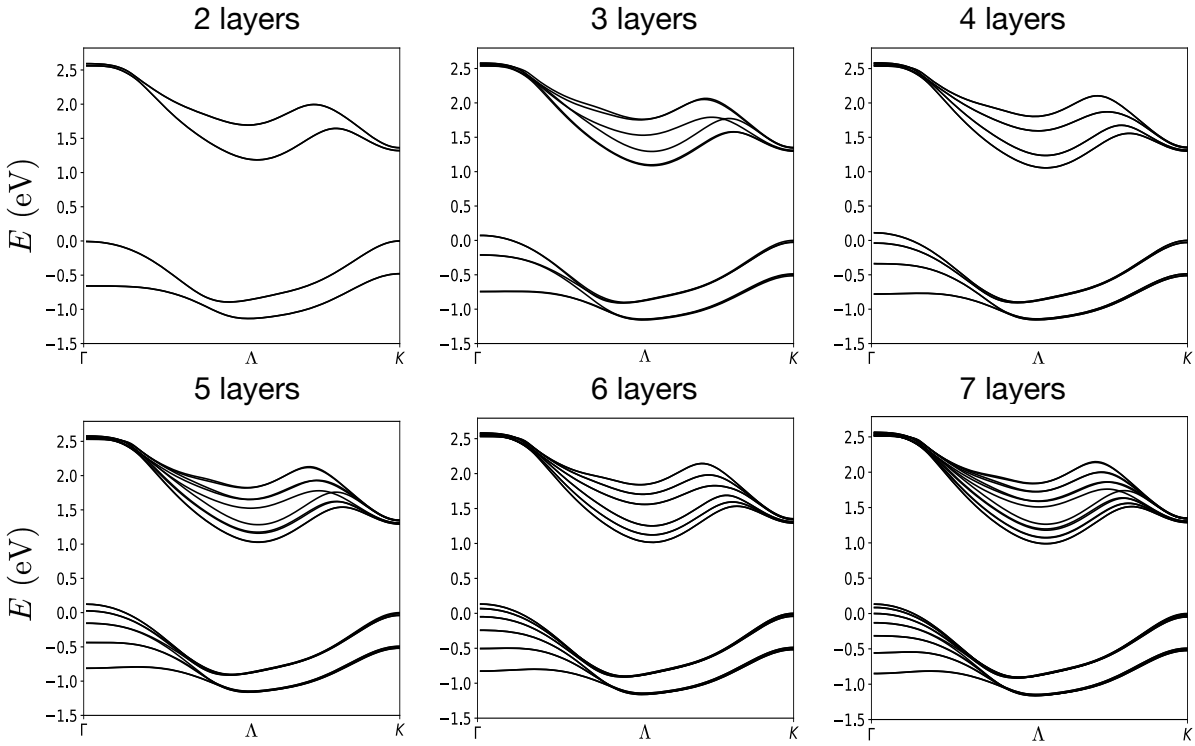

Figure S6: DFT band structure calculations for $\mathrm{WSe_2}$ crystals with *N* = 2–7 layers. Shown are the highest valence subbands and lowest conduction subbands between the Γ and K points of the Brillouin zone.

We adopted a Methfessel-Paxton smearing of 0.005 Ry and set the total energy convergence to less than 10^{-6} eV in all calculations. Spin–orbit coupling was included in all electronic band structure calculations. To eliminate spurious interactions between adjacent supercells, a 20 Å vacuum buffer space was inserted in the out-of-plane direction. The interlayer separations is taken to be the experimental values, with $d_{\mathrm{WSe_2}} = 6.477$ Å (*4*).

Fig. S6 shows the obtained band structures for $\mathrm{WSe_2}$ flakes with $N = 2 - 7$ layers. The valence and conduction band edges are found at the Γ and Λ points, respectively, showing splitting into multiple subbands. This is due to the orbital compositions of the respective monolayer bands. The valance band at the Γ–point is dominated by the metal d_{z^2} orbital and the conduction band at the Λ–point contains both chalcogen p_z and metal d_{z^2} orbitals (*5*), resulting in the strong

interlayer coupling and splitting of the bands into multiple subbands and the transition from a monolayer direct gap ($K-K$) to a multilayer indirect gap ($\Gamma-\Lambda$). At the Γ–point valence subbands we find N subbands for N layers, with each subband being spin degenerate due to time reversal symmetry. At the Λ–point conduction subbands, the combination of the 2H–stacking and spin–orbit coupling result in an alternating subband structure for even and odd number of layers. For even N, spatial inversion symmetry results in N spin–degenerate subbands, whereas for odd N, the lack of spatial inversion symmetry results in $2N$ spin–polarized subbands.

A complementary description of the subband structures can be obtained from the limit of many layers ($N \gg 1$). We consider the bulk dispersion near the valence band edge, found at the Γ–point with $k_z = 0$ (Fig. S7), given by

$$\epsilon(k_z, \mathbf{k}) = -\frac{\hbar^2 k_z^2}{2m_{v,z}} - \frac{\hbar^2 k_{xy}^2}{2m_{xy}}(1 + \zeta k_z^2), \tag{1}$$

where k_z is the out–of–plane wave vector and k_{xy} is the in–plane wave vector. The dispersion parameters are: the effective mass in the z–direction $m_{v,z} = 1.08m_0$, the in–plane effective mass $m_{xy} = 0.70m_0$, both given in terms of the free electron mass m_0 and were obtained by fitting the bulk dispersions Fig. S7, and $\zeta = -5.45$ Å^2, is a parameter related to the non–linearity of the in–plane dispersion.

For a finite size crystal we have the following generalized boundary conditions at the top and bottom layers for the electronic wave function $\psi(z)$, along the z–direction in the crystal,

$$\left[\pm\nu d\partial_z\psi(z) + \psi(z)\right]_{z=\pm L/2} = 0, \tag{2}$$

where d is the interlayer distance, L is the crystal size, ν is a dimensionless parameter of order 1, and the $\pm$ correspond to the top and bottom layers, respectively (see Fig. S8). The physical origin of the parameter ν in the boundary condition is to allow the node of the wave function to

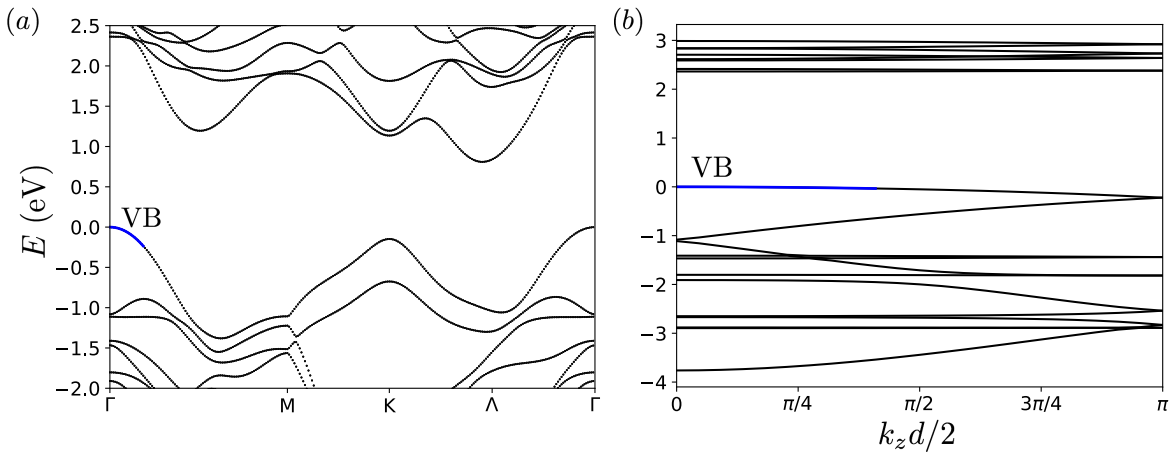

Figure S7: DFT calucaltion for bulk WSe_2 showing **a** In–plane dispersion (black points) and **b** out–of–plane dispersion along $\Gamma - A$ (black lines). The solid blue line shows the fitted in–plane and out–of–plane fittings for the effective mass near the Γ–point.

be shifted away from the centre of the layer, taking into account the band's orbitals extension in the z–direction. In particular, the condition $\psi(\delta) = 0$ for small δ translates following expansion to $\psi(0) + \delta\partial_z\psi(0) = 0$, which is the form of the boundary condition.

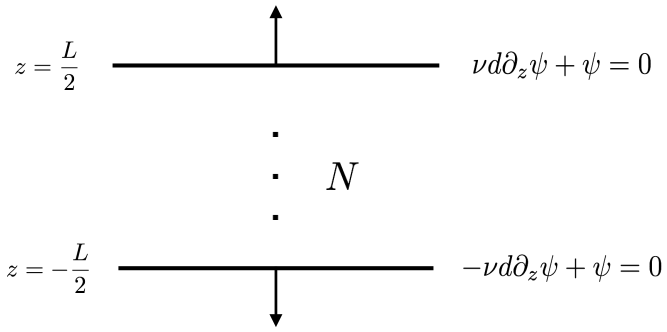

Figure S8: General boundary conditions on the top and bottom layers for a second order differential equation for finite size crystal with N layers, interlayer distance d, and total size L.

The general solution to the one–dimensional, time–independent Schrödinger equation in the crystal is given by travelling waves,

$$\psi(z) = ve^{ik_z z} + ue^{-ik_z z}. \tag{3}$$

Inserting Eq. 3 into the generalized boundary conditions in Eq. 2 and solving for k_z we get,

$$1 = e^{2i[Lk_z + 2\arctan(\nu d k_z)]}. \tag{4}$$

This gives the quantization condition for k_z in the finite size crystal,

$$Lk_z + 2\arctan(\nu d k_z) = \pi j. \tag{5}$$

For the top most subbands with large number of layers we have $k_z \sim 1/L \ll 1/d$, such that we can approximate the second term as $\arctan(x) \sim x$, finally giving the quantization relation for k_z,

$$k_z = \frac{\pi j}{d(N + 2\nu)}. \tag{6}$$

Inserting Eq. 6 into the bulk dispersion Eq. 1, gives the description of the valence edge subbands energies and dispersions,

$$E_{j|N}(k) = \frac{\hbar^2}{2m_z}\frac{\pi^2 j^2}{d^2(N+2\nu)^2} + \frac{\hbar^2 k_{xy}^2}{2m_{xy}}\left[1 + \frac{\zeta\pi^2 j^2}{d^2(N+2\nu)^2}\right]. \tag{7}$$

Using Eq. 7 we obtain the intersubband transition energies at the Γ–point. In particular, we obtain the formula for the main intersubband transition given in the main text,

$$E_{1|N} - E_{2|N} = \frac{3\pi^2\hbar^2}{2m_z d^2(N+2\nu)^2}. \tag{8}$$

The subband in–plane dispersions are described by the second term in Eq. 7, with the subband effective masses as a function of number of layers given by,

$$m_{j|N}^{-1} = m_{xy}^{-1}\left[1 + \frac{\zeta\pi^2 j^2}{d^2(N+2\nu)^2}\right]. \tag{9}$$

In Fig. S9a,b we show the transition energies and effective masses near the valence subbands

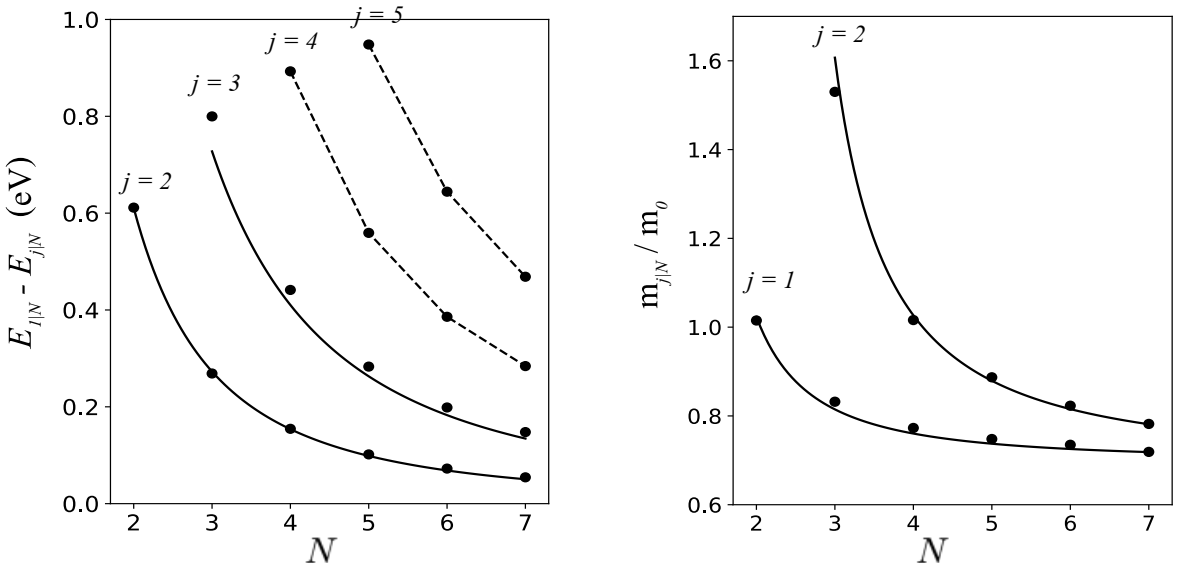

Figure S9: **a**, Transition energies from the first subband to next few subbands as a function of number of layers. The $1|N \rightarrow 2|N$ was fitted to Eq. 8, giving $\nu = 7 \times 10^{-3}$. The formula was then used to plot the solid line for the $1|N \rightarrow 3|N$ transition. **b**, Subbands effective masses as a function of number of layers obtained from DFT (Black dots) for the first two subbands, and the fitting to the model Eq. 9 (solid black lines).

edge as a function of number of layers obtained form the DFT calculations, and the fittings to the model Eqs. 8, 9. The good agreement between the model and DFT data strongly support the validity of our theoretical analysis.

II Line shape of intersubband absorption

In this section we obtain the line shape resulting from the intersubband absorption of out–of–plane polarized light. The subband states wave functions and in–plane dispersions which are necessary in order to obtain the optical matrix elements and absorption rates, are taken from the **k**·**p**-tight binding model developed in (*6*).

The optical matrix element is given by the out–of–plane dipole moment $d_z = e\langle 2|z|1\rangle$, given by the matrix element of the z coordinate operator between the two subband states. In particular,

focusing on p–doped 2H–stacked TMDs, the main intersubband transition is between the first and second $(1 \to 2)$ top most valence subbands having opposite parities under spatial (even N) or mirror reflection (odd N) symmetry operations, while the $1 \to 3$ transition is forbidden due to the same parity of the subband states.

The valence band intersubband absorption line shape is obtained using Fermi's Golden rule,

$$\tau^{-1}(\hbar\omega) = \frac{2\pi}{\hbar} g_s |E_z(\hbar\omega) d_z|^2 \sum_{\mathbf{k}} f(\mathbf{k}) \delta(E_2(\mathbf{k}) - E_1(\mathbf{k}) - \hbar\omega), \tag{10}$$

where $E_z(\hbar\omega)$ is the out–of–plane electric field component of the incoming light of energy $\hbar\omega$, $g_s = 2$ is the spin degeneracy, $f(k)$ is the carrier distribution function, taken to be the Boltzmann distribution for lightly p-doped sample at room temperature. The delta function ensures energy conservation for the transition between the two subbands with parabolic dispersions with given effective masses, $E_j(\mathbf{k}) = E_j(0) - \frac{\hbar^2 k_{xy}^2}{2m_j}$. For the valence subbands in 4–layers WSe_2, we obtain for the effective masses $m_1 = 0.76 m_0, m_2 = 1.14 m_0$ given in terms of the free electron mass, and $E_2(0) - E_1(0) = 154\ \mathrm{meV}$ for the intersubband energy spacing.

We use a constant value for the optical matrix element d_z, dependent only on the number of layers N. We have evaluated the dependence of d_z on in–plane momentum within the framework of the quantum well model discussed in Section I.2 and found a variation of less than 5% within all relevant momentum ranges, determined by temperature, the Fermi momentum, and the tip curvature (see Section II.1 below). This justifies our approximation.

The resulting line shape is then given by the analytical form,

$$I(\hbar\omega) \propto \frac{4\pi\mu\hbar\omega n_h}{m_1 k_B T} |d_z|^2 e^{-\frac{\mu}{m_1 k_B T}(E_2 - E_1 - \hbar\omega)} \Theta(E_2 - E_1 - \hbar\omega), \tag{11}$$

where k_B is the Boltzmann constant, n_h is the carrier density, $1/\mu = 1/m_1 - 1/m_2$, and the Heaviside function restricts the photon energies to be smaller than the intersubband energy

spacing, due to the subband dispersions. The different subband effective masses result in a thermally broadened absorption line shape with broadening given by

$$\Gamma \approx \left(1 - \frac{m_1}{m_2}\right) \max\{\epsilon_F, k_B T \log 2\}, \tag{12}$$

where ϵ_F is the Fermi energy. At room temperature and for low doping levels this results in a broadening of $\Gamma = 5.9\ \mathrm{meV}$ for 4–layer WSe_2.

II.1 Line broadening due to tip curvature

The effect of the tip on the allowed intersubband transitions and the resulting line shape is modelled using the Fourier transform of the z–component of the tip's electric field, which is coupled to the intersubband transitions (*7*). The tip form factor is given in terms of the wave vector $\boldsymbol{\xi}$ as,

$$\rho_{\mathrm{tip}}(\boldsymbol{\xi}) = \frac{1}{12\pi\xi_0^4}\xi^2 e^{-\xi/\xi_0}, \tag{13}$$

where $\xi_0 = \frac{\pi}{a_{\mathrm{tip}}}$, with a_{tip} the tip radius. The nominal tip radius of the AFM tips used in the experiment is $a_{\mathrm{tip}} < 10$ nm. However, a SEM image (Figure S10a) of a typical tip used in our experiments shows $a_{\mathrm{tip}} \approx 12$ nm, which we use for our calculations. We note that smaller features can occur due to smaller Pt grains at the AFM tip apex and smaller a_{tip} leads to both a larger line width broadening and blue-shift. The presence of the tip relaxes the crystal momentum conservation allowing for non-vertical optical transitions. In the presence of the tip, Eq. 10 giving the absorption line shape, is modified as follows,

$$\tau^{-1}(\hbar\omega) = \frac{2\pi}{\hbar} g_s |E_z(\hbar\omega) d_z|^2 \sum_{\boldsymbol{\xi},\mathbf{k}} \rho_{\mathrm{tip}}(\boldsymbol{\xi}) f(\mathbf{k}) \delta(E_2(\mathbf{k}+\boldsymbol{\xi}) - E_1(\mathbf{k}) - \hbar\omega). \tag{14}$$

The resulting line shape shown in the main text is obtained by numerical integration.

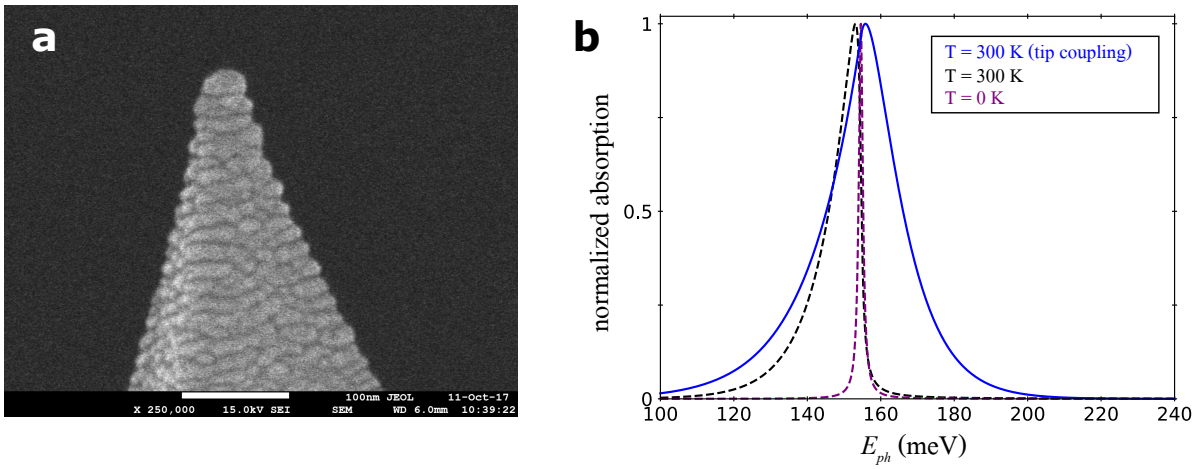

Figure S10: **a**, SEM image of an AFM tip as used in our experiments. Image provided by NanoWorld AG. **b**, Calculated line shapes at different temperatures. The blue lines also takes into account the tip coupling with $a_{\mathrm{tip}} = 12$ nm.

II.2 Line broadening due to intersubband electron-phonon relaxation

Intersubband relaxation through optical phonons results in broadening of the absorption line shapes, governing the line width at low temperatures. The phonon broadening is introduced by replacing the delta function in Eq. 10 by a Lorentizan,

$$L(\hbar\omega) = \frac{1}{\pi} \frac{\gamma}{(E_2(k) - E_1(k) - \hbar\omega)^2 + \gamma^2}, \tag{15}$$

with γ the phonon-induced broadening.

We consider the contribution of three optical phonon modes taken to have a constant dispersion, homopolar HP (A_1'), longitudinal LO (E'), and out of plane ZO (A_2''), with the corresponding irreducible representations of $D_{3\mathrm{h}}$ point group given in parenthesis. The detailed derivation of the multilayer electron–phonon couplings is given in (*8*).

To model the multilayer phonon modes, we approximate the phonons in each layer to be degenerate and independent, allowing to form linear combinations of the phonons in each layer, forming N modes for a given phonon type (HP, LO and ZO), with N the number of layers. The

carrier in a given subband state has components on all layers, such that the intersubband phonon scattering matrix element is given by the coupling of the carriers component on each layer with the phonons in all layers,

$$M_{\mu,\nu}(\mathbf{q}) = \frac{1}{\sqrt{N}} \sum_{n} g_{\mu}(\mathbf{q}) f_{\nu}(n) c^{*}_{1,n}(\mathbf{q}) c_{2,n}(0). \tag{16}$$

The summation is taken over the number of layers N, $g_{\mu}(q)$ is the carrier-phonon coupling for the given phonon mode μ with wave vector $\mathbf{q}$, $c_{j,n}(\mathbf{k})$ is the amplitude of the carrier wave function in subband j with wave vector $\mathbf{k}$ on layer n, and $f_{\nu}(n)$ is the phase of the given multilayer phonon mode on layer n, ($\nu = 1, .., N$). The broadening is given by $\gamma = \hbar/\tau$, with the total scattering rate given by Fermis golden rule,

$$\begin{aligned} \tau^{-1} &= \frac{m_1}{\hbar^2} \sum_{\mu,\nu} |M_{\mu,\nu}(q_*)|^2 \Theta(E_2 - E_1 - \hbar\omega_{\mu})[1 + n(\hbar\omega_{\mu})]; \\ q_* &= \sqrt{\frac{2m_1}{\hbar^2}(E_2 - E_1 - \hbar\omega_{\mu})}. \end{aligned} \tag{17}$$

Here the summation is over the three phonon modes $\mu =$ HP, LO and ZO, with $\hbar\omega_{\mu}$ the phonon energy and $n(\hbar\omega_{\mu}) = \frac{1}{e^{\hbar\omega_{\mu}/k_B T} - 1}$, is the phonon occupation given by the Bose-Einstein distribution. The summation over ν corresponds to the N multilayer phonon modes for a given phonon μ, with electorn–phonon matrix element $M_{\mu,\nu}(q)$, and the Heaviside function restricts the phonon induced intersubband relaxation such that the phonon energy must be smaller than the intersubband energy spacing. The energy conservation in the scattering process sets the emitted phonon wave vector to be q_*.

The carrier–phonon coupling for the HP phonon mode is modelled through the phonon induced deformation potential, $D = 2.2\mathrm{eV/\AA}$ for Γ–point holes in monolayer $\mathrm{WSe_2}$ (*9*). The LO phonon mode coupling is modelled through the phonon induced electrostatic potential due to the polar nature of the material and the in-plane Born effective charge $Z = -1.08$ for $\mathrm{WSe_2}$

(*8*), similarly the ZO phonon coupling is modelled through the phonon induced out-of-plane dipole, with the out of plane Born effective charge, $Z_z = -0.12$ for $\mathrm{WSe_2}$ (*10*). The resulting broadening of $\gamma = 0.66\ \mathrm{meV}$ quoted in the main text is obtained by summing the contribution of the HP, LO and ZO phonons in 4–layer $\mathrm{WSe_2}$.

III Thin film inversion model

In order to extract $\epsilon_{\mathrm{WSe_2}}$ from the measured s-SNOM data we use a thin-film inversion model as described by Govyadinov and co-workers (*11*). The model expands the general tip-sample interaction into a Born series for the special case of a thin-film sample (WSe_2) on top of an infinitely thick substrate (HfO_2). For our analysis we limit ourselves to zeroth and first order terms. The Born series expansion allows us to decouple the optical signals from WSe_2 and HfO_2, and to expand the effective polarizability of the AFM tip above the WSe_2–HfO_2 system into a Taylor series

$$\alpha_{\mathrm{eff}} = \sum_{k=0}^{\infty} \alpha_k \beta_{\mathrm{WSe_2}}^k, \tag{18}$$

where $\beta_{\mathrm{WSe_2}} = \frac{\epsilon_{\mathrm{WSe_2}}-1}{\epsilon_{\mathrm{WSe_2}}+1}$ is the quasistatic reflection coefficient at the surface with the bulk permittivity $\epsilon_{\mathrm{WSe_2}}$, and α_k are the expansion coefficients, which are independent of $\epsilon_{\mathrm{WSe_2}}$ but depend on the thickness of the WSe_2 sample. We can now calculate the normalized optical s–SNOM signal at the n-th harmonic – η_n – by taking the Fourier transform defined as $\hat{F}_n[X(t)] = \int X(t)\mathrm{e}^{in\Omega t}\mathrm{d}t$, with Ω the tip frequency and normalizing it to the reference effective polarizability of the AFM tip above the HfO_2 substrate

$$\eta_n = \sum_{k=0}^{\infty} \beta_{\mathrm{WSe_2}}^k \frac{\hat{F}_n[\alpha_k]}{\hat{F}_n[\alpha_{\mathrm{eff,HfO_2}}]}. \tag{19}$$

By truncating this expansion at a particular order K (for our analysis we use $K = 21$), $\beta_{\mathrm{WSe_2}}$ and η_n are related by a simple polynomial equation and therefore $\epsilon_{\mathrm{WSe_2}}$ can be computed from

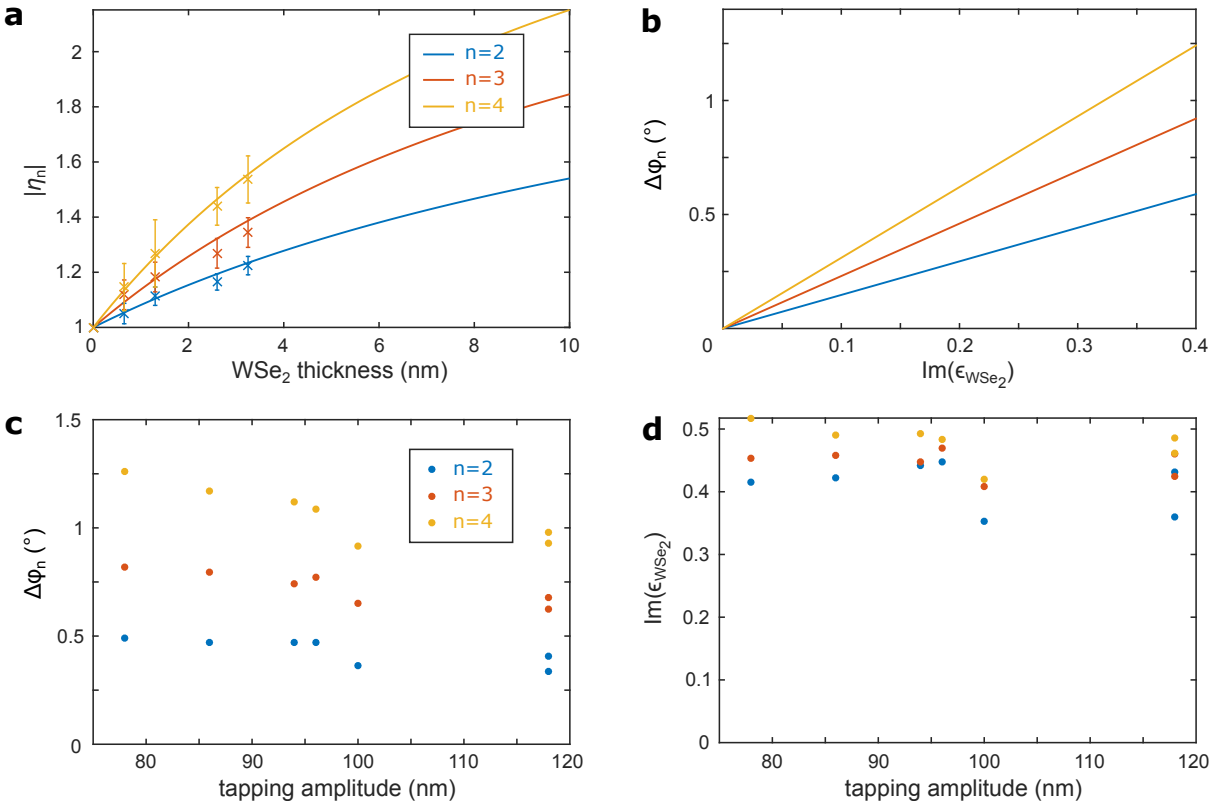

Figure S11: **a**, Simulation of the absolute value of the optical signal $|s_n|$ for different thicknesses of a WSe_2 flake ontop of a HfO_2 substrate. Shown are the demodulation orders n = 2,3,4. We use a thin-film inversion model (*11*) employing a tip frequency $\Omega = 250$ kHz and oscillation amplitude A = 75 nm, values that are typically used in experiment. The used permittivities are ϵ_{HfO_2} = 2.8 and ϵ_{WSe_2} = 7.3. Crosses indicate the experimental values, obtained on the flake shown in Figure 2 of the main text at E_{ph} = 165 meV. Error bars indicate the root mean square in the analysed areas of the flake. **b**, Simulated change in the phase of the optical signal $\Delta\varphi_n$ as a function of $Im(\epsilon_{WSe_2})$ for a 4-layer thick WSe_2 flake on top of HfO_2 at E_{ph} = 165 meV. **c**, $\Delta\varphi_n$ for different tapping amplitudes and demodulation orders measured on a 5-layer thick WSe_2 flake on top of a SiO_2 substrate at E_{ph} = 117 meV. **d**, The obtained $Im(\epsilon_{WSe_2})$ from the data in **c** using the thin-film inversion model.

the measured optical signal.

In order to verify this model we first simulate the expected optical signal of a WSe_2 flake with varying thicknesses on top of an infinitely thick HfO_2 substrate and compare the simulations to our measurements. We employ simulation parameters that we typically use in our

experiments, namely an AFM tip oscillation amplitude $A = 75$ nm and tip frequency $\Omega = 250$ kHz. Input parameters are ϵ_{WSe_2} and the permittivity of the underlying HfO_2, $\epsilon_{HfO_2} \approx 2.8$ at $E_{ph} = 165$ meV (*12*). Since WSe_2 has a highly anisotropic permittivity with an in-plane component $\epsilon_{WSe_2,xy} = 12.7$ and an out-of-plane component $\epsilon_{WSe_2,z} = 4.2$ (*13*) we use an effective permittivity $\epsilon_{WSe_2} = \sqrt{\epsilon_{WSe_2,xy} \times \epsilon_{WSe_2,z}} = 7.3$ for all our simulations. The absolute value of the optical signal $|s_n|$ normalized to the signal on HfO_2 is shown in Figure S11a for demodulation order n = 2,3,4. We observe a monotonic, sublinear increase with thickness for all demodulation orders. This effect comes from the change in the dielectric environment experienced by the the near-field around the AFM tip. In first approximation, $|s_n|$ corresponds to the quasi-static reflection coefficient, which is larger for WSe_2 than HfO_2. We find a good agreement between the simluated optical signal and the s-SNOM measurements on the sample presented in Figure 2 of the main text, confirming the validity of the thin-film inversion model for our samples.

Next, we model how absorption in WSe_2 and therefore a change in *Im*(ϵ_{WSe_2}) is reflected in the measured s-SNOM signal. For this we assume a 4-layer thick WSe_2 flake on top of HfO_2 at E_{ph} = 165 meV. The change in phase of the optical signal $\Delta\varphi_n$ is plotted in Figure S11b. We observe a linear increase with *Im*(ϵ_{WSe_2}) for all demodulation orders. $|s_n|$ does not depend significantly on *Re*(ϵ_{WSe_2}) (not shown). Therefore, for a given layer thickness, $\Delta\varphi_n$ provides a direct measure of the absorption for all relevant absorption values of this experiment.

Finally, we verify that the reconstruction of *Im*(ϵ_{WSe_2}) from the optical signal using the thin-film inversion model is independent of any used measurement parameters. To do so we measure one of our samples for different tapping amplitudes and record different demodulation orders n = 2,3,4 (Figure S11c). First, we observe a distinctively larger $\Delta\varphi_n$ for higher demodulation orders n. Second, we observe a slight decrease of $\Delta\varphi_n$ with tapping amplitude, especially for higher n. These features should not appear in the obtained *Im*(ϵ_{WSe_2}), as they do not represent any physical properties of the probed WSe_2 flake. Indeed, after the inversion using the thin-film

model (Figure S11d) we see that $Im(\epsilon_{WSe_2})$ shows no more dependence on the used tapping amplitude. We also observe that the difference between different demodulation orders reduces drastically, although it does not vanish completely.

IV Doping modulation

We modulate the doping of the TMD flake by modulating the applied backgate voltage V_{BG} between the Si wafer and the TMD flake across a substrate oxide. In order to monitor the doping of the TMD flake we constantly apply a small bias voltage $V_{bias} \approx 0.02$ V between two contacts evaporated on the TMD flake and monitor the flowing current. For the WSe_2 flake presented in the main text we observe a field effect transistor effect with exponentially increasing current for negative V_{BG}, as is typical for a p-doped semiconductor (Figure S12a). This demonstrates that V_{BG} indeed dopes the WSe_2 flake. During all the modulation measurements presented in the main text we also recorded the current flowing between the two contacts. Figure S12b shows a time trace of the measured current during the xy scan presented in Figure 2d of the main text, where V_{BG} was modulated between -5 and 0 V. We clearly see that the doping of the flake is modulated between p-doping and depletion. We use this measured current as a reference to determine when the flake was p-doped. The recorded signal shows discrete points since each pixel of the s–SNOM measurement has a finite integration time, which was set to 19.7 ms for the data shown. We define an upper and lower bound for the measured current - typically 28 and 3 nA - and points that lie in between these two boundaries are discarded from the measurement since one part of them was recorded when the flake was p-doped and the other part when it was charge neutral.

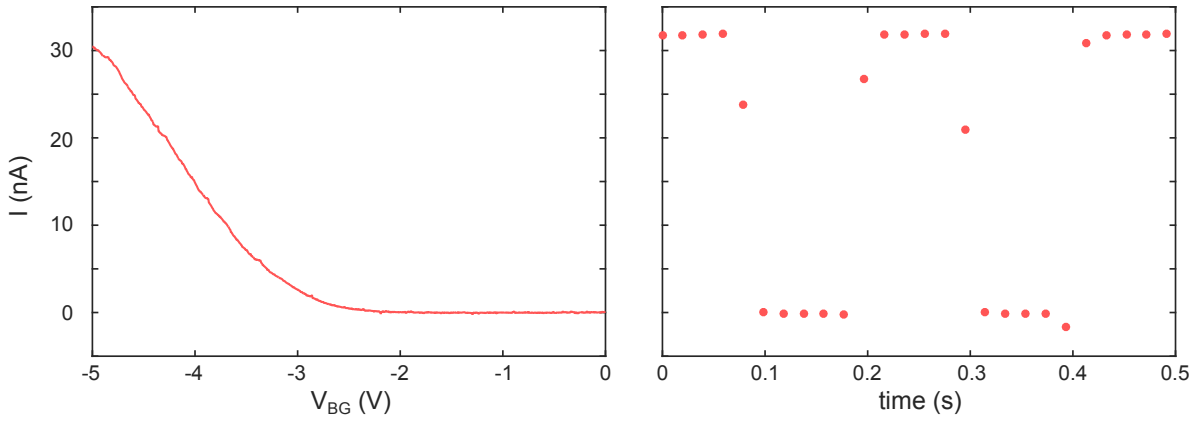

Figure S12: **a** Measured current for the WSe_2 flake presented in the main text with V_{bias} = 0.02 V as a function of V_{BG}. **b** Measured current during the xy scan presented in Figure 2d of the main text on the same WSe_2 flake as presented in **a**. V_{BG} was modulated between -5 and 0 V. The integration time per pixel was set to 19.7 ms.

V Drude model

In our s–SNOM experiment we measure the complex permittivity of the sample at $E_{ph} = \hbar\omega$, with $\hbar$ being the reduced Planck constant and ω the light angular frequency. However, the complex permittivity of any material that contains free charge carriers varies with ω. This can be seen by looking at the complex conductivity $\sigma(\omega)$ derived from the Drude model:

$$\sigma(\omega) = \frac{D}{1/\tau - i\omega}, \tag{20}$$

with the Drude weight $D = \frac{n_{3D}e^2}{m_{xy}}$, where n_{3D} is the material's charge carrier density (in units 1/m^3), m_{xy} its in-plane effective mass, and e the electron charge. The scattering time τ is given as $\tau = \frac{\mu m_{xy}}{e}$, with μ the charge carrier mobility. The Drude component of the material's (complex) relative permittivity ϵ_{Drude} is related to $\sigma(\omega)$ as

$$\epsilon_{\text{Drude}}(\omega) = i\frac{\sigma(\omega)}{\epsilon_0\omega}, \tag{21}$$

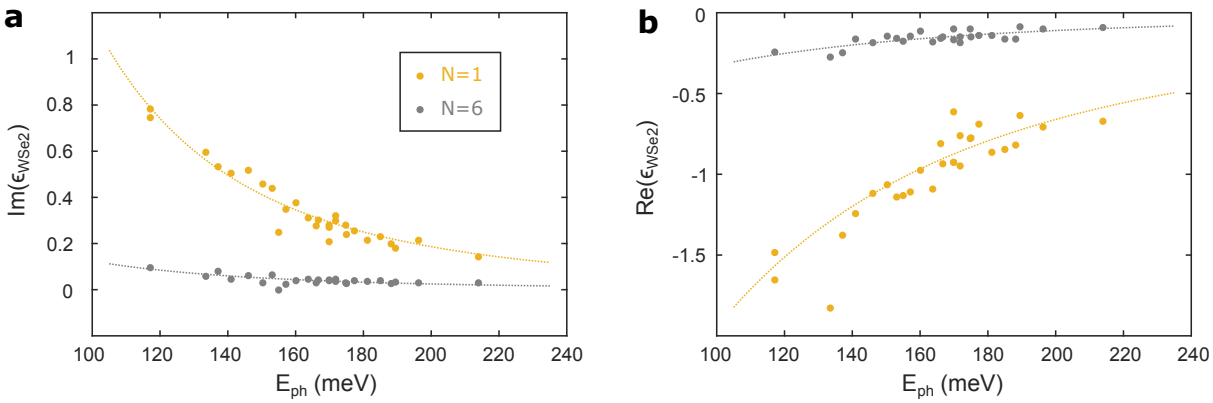

Figure S13: **a,** Obtained $Im(\epsilon_{WSe_2})$ as a function of E_{ph} for N = 1 (yellow) and N = 6 (grey). The observed behavior can be well described by fitting a Drude model (dashed lines). The data is taken from the main text (Figure 3a), where N = 1 is not shown. **b,** Change in $Re(\epsilon_{WSe_2})$ for the same data as in **a**. Dashed lines show the Drude fit.

with the vacuum permittivity ϵ_0.

layer numbers	fitted data	D in 10^{15} S/sm	τ in fs	n_{2D} in 10^{11} cm^{-2}	μ in cm^2/Vs
N = 1	Re(ϵ_{WSe_2})	6±1	11±6	$8.8^{+1.2}_{-1.5}$	30±16
	Im(ϵ_{WSe_2})	5.3±1.2	10^{+4}_{-3}	7.8±1.8	28^{+10}_{-9}
N = 6	Re(ϵ_{WSe_2})	1.0±0.3	9±7	11^{+4}_{-3}	20±15
	Im(ϵ_{WSe_2})	0.5±0.1	7±4	5.6±1.4	15^{+8}_{-9}

Table S1: Parameters obtained from the Drude fit to the data in Figure S13

We can now fit $\epsilon_{\text{Drude}}(\omega)$ to the data presented in Figure 3a of the main text for all N that do not show a resonance due to intersubband transitions. In the investigated range of E_{ph} these are the N = 1 (not shown in the main text) and N = 6 areas of the WSe_2 flake. $Im(\epsilon_{WSe_2})$ and $Re(\epsilon_{WSe_2})$ together with the Drude fits are shown in Figure S13a and b. Each fit contains two free fitting parameters, D and τ, whose obtained values are listed in Table S1. We now assume an effective in–plane hole masses of $m_{xy,N=1} = 0.64$ m$_0$ (*14*) for N = 1 (at the K point of the

Brillouin zone) and $m_{xy,N=6} = 0.82$ m_0 (*15*) for N = 6 (at the Γ point). Furthermore, we can assume that V_{BG} induces a constant sheet carrier density n_{2D} so that $n_{3D} = n_{2D}/Nd$, where d is the thickness of a single WSe_2 layer. This allows us to express D and τ in terms of the hole mobility μ and sheet carrier density n_{2D}. The obtained values are given in Table S1 with their corresponding 90% confidence values from the fit. We find hole mobilities that are consistent with previously reported values (*16*) and sheet carrier densities that agree well with capacitance measurements performed on a separate device, yielding n_{2D} = 9x10^{11} cm^{-2}. This confirms that we can accurately model the Drude response of our device.

In order to account for the Drude contributions in the layer numbers that additionally show intersubband absorbtion (N = 4 and N = 5), we use the same fitting parameters as obtained from the fit to the N = 6 data and the relationship $n_{3D} = n_{2D}/Nd$. In this way we can extend the N = 6 fit to the N = 4 and N = 5 data without introducing any new fitting parameters.

VI Spatial variances

The spatial resolution of our experiment of ≈20 nm allows us to investigate spatial variances of the absorption, which could be an indication of substrate-induced disorder or disorder within the TMD flake. However, within the signal to noise ratio of our experiment we cannot observe significant spatial variances of the optical signal for the investigated ranges of E_{ph} (Figure S14). We furthermore do not observe correlations in the spatial absorption for different E_{ph}, indicating that any observed spatial variances can be attributed to noise.

VII Tip-induced doping

It has been reported previously that scanning a charged AFM tip over a 2D electron gas locally influences its charge carrier density (*17, 18*). For the data shown in Figure 4b and c of the main

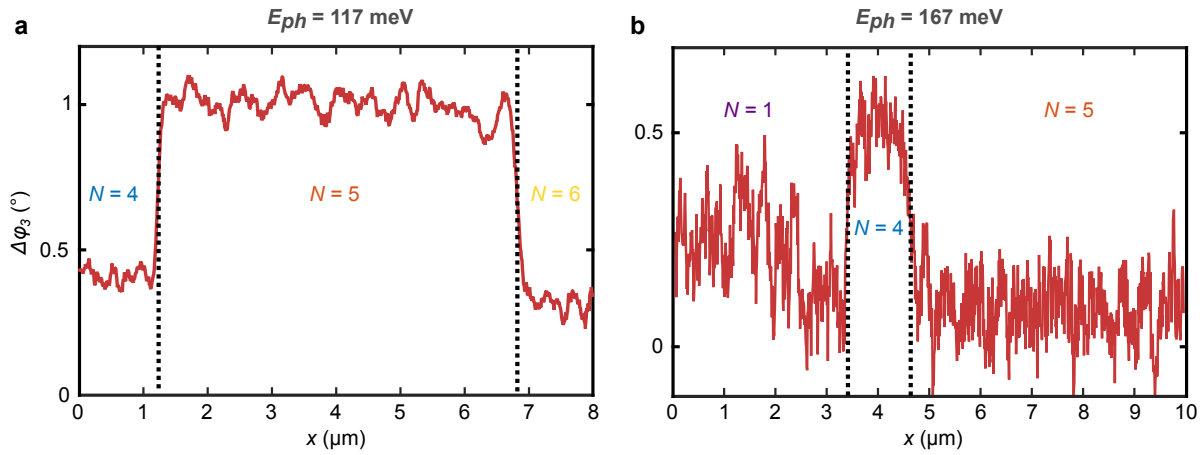

Figure S14: **a, b,** Line traces of $\Delta\varphi_3$ measured for E_{ph} = 117 meV (**a**) and E_{ph} = 167 meV (**b**). The resonant layers are N = 5 in **a** and N = 4 in **b**

.

text, we used this effect in order to locally dope the 2D material quantum well and enhance its intersubband absorption. We apply a constant voltage V_{tip} to the 2D crystal, which locally induces charge carriers (holes for $V_{\text{tip}} > 0$ and electrons for $V_{\text{tip}} < 0$) due to the coupling with the grounded, metallic AFM tip. We can furthermore apply a backgate voltage V_{BG}, globally controlling the charge carrier density. In order to estimate the magnitude of the tip-induced doping we perform s-SNOM measurements on a separate graphene flake exfoliated on a Si/SiO_2 substrate and make use of the fact that the optical signal s_4 measures the local complex permittivity underneath the tip. At the graphene charge neutrality point the imaginary part of the permittivity and therefore *Im*(s_4) has a minimum, while *Re*(s_4) has a maximum. We now vary V_{BG} and record s_4 for different voltages V_{tip} applied to the graphene flake. For V_{tip} = 0 (Figure S15a) we see that the charge neutrality point of graphene is at about V_{BG} = 10 V, indicating that the graphene flake is slightly hole doped. For V_{tip} = -1.5 V the *local* charge neutrality point of graphene shifts to negative V_{BG}, indicating that the graphene flake becomes locally electron doped due to the interaction with the AFM tip. We repeat this measurement for various V_{tip} and find that V_{tip} influences the local charge carrier density of graphene as $V_{\text{tip}} \approx$ -20 V_{BG}.

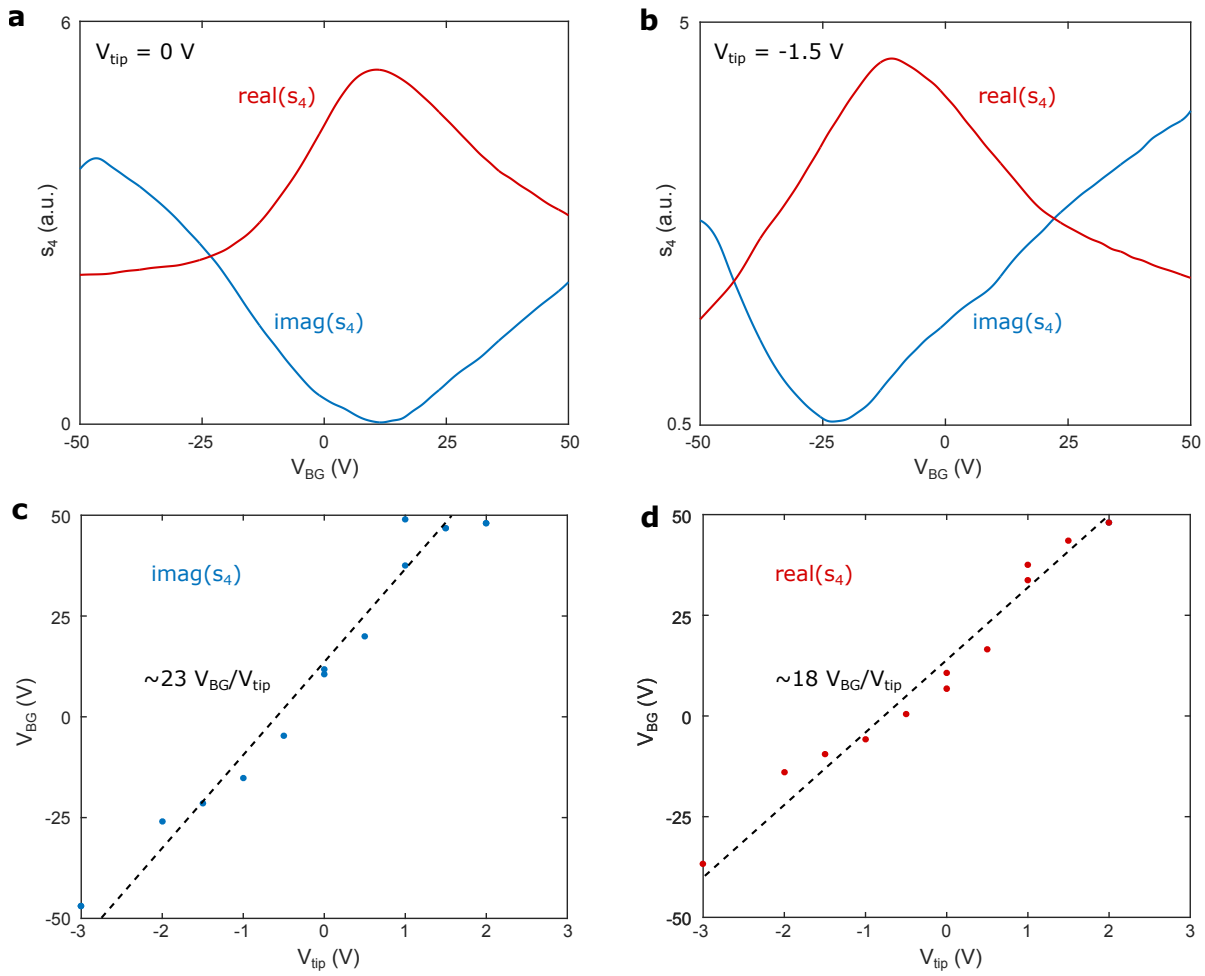

Figure S15: **a, b,** Measured complex optical signal s_4 corresponding to the local complex conductivity of graphene underneath the AFM tip for V_{tip} = 0 V (**a**) and V_{tip} = -1.5 V (**b**). **c, d** Minimum of $Im(s_4)$ (**c**) and maximum of $Re(s_4)$ (**d**) obtained from measurements as in **a** and **b** for different V_{tip}. The dashed lines are linear fits to the data, whose slope indicate the needed V_{BG} in order to compensate for the effect of V_{tip}.

VIII Calculation of the absorption

In order to calculate the 2D sheet absorption α_{2D} from the obtained relative permittivity ϵ_{WSe_2} we first calculate the complex refractive index

$$N = \sqrt{\epsilon_{WSe_2}}.$$

Its imaginary part *Im*(N) = κ is related to the attenuation coefficient μ as

$$\mu = 4\pi\kappa/\lambda,$$

with λ the illumination wavelength. Using the Beer-Lambert law we then obtain for small absorption

$$\alpha_{\mathrm{2D}} = 1 - \mathrm{e}^{-\mu d} \approx \mu d.$$

IX Measurements on a MoS_2 flake

Intersubband transitions are not limited to WSe_2 but can be observed in any semiconducting 2D material. To demonstrate this, we performed measurements on a MoS_2 flake, exfoliated on a Si/SiO_2 substrate. The flake consists of several terraces with layer numbers N = 2, 3, 5, 7 and larger, which we identify by a combination of optical contrast and AFM measurements (Figure S16a). In order to observe intersubband transitions we perform two scans over the same region, one with V_{BG} = -50 V and the other one with V_{BG} = +50 V, and record the optical signal at E_{ph} = 117 meV. Since MoS_2 is intrinsically n-doped, V_{BG} = -50 V shifts the doping towards charge neutrality, while V_{BG} = +50 V increases the electron doping. We now subtract the two scans and look at the difference in phase of the fourth harmonic of the tip frequency, $\Delta\varphi_4$, which is proportional to the absorption that is induced by increasing electron doping (Figure S16b). We clearly observe enhanced absorption in the N = 5 area of the flake, which we attribute to intersubband transitions and is consistent with our theoretical calculations (from band structure calculations we obtain $E_{\mathrm{sub}} = 113$ meV and $E_{\mathrm{sub}} = 119$ meV for the two different spin polarizations, respectively). In order to support this observation we study the doping dependence of the observed resonance. We perform several line scans for different V_{BG} and average the obtained $\Delta\varphi_4$ for each layer number. Due to Drude absorption we observe an

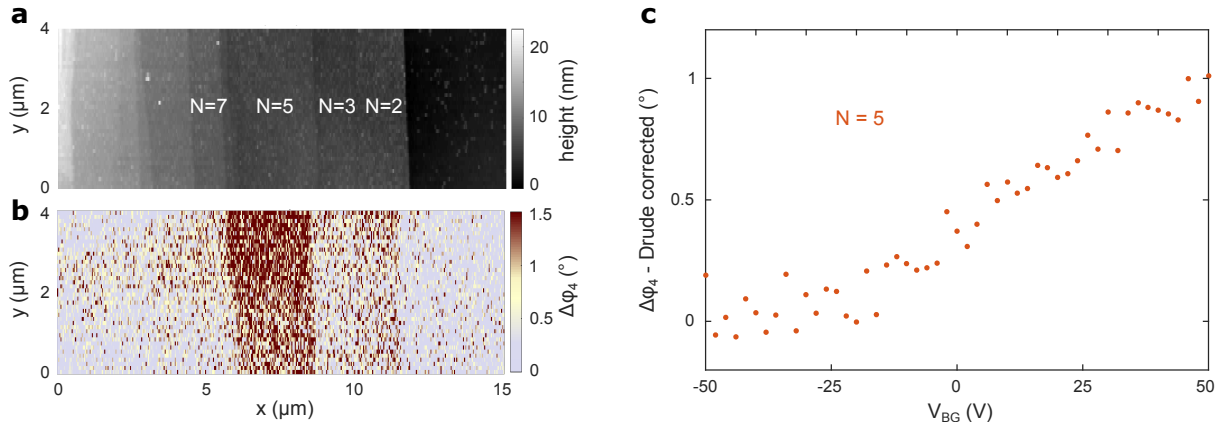

Figure S16: **a,** AFM image of a terraced MoS_2 flake exfoliated on a Si/SiO_2 substrate. Layer numbers are indicated for clarity. **b,** $\Delta\varphi_4$, which is proportional to the absorption with increasing electron density, measured at E_{ph} = 117 meV on the same area of the flake as in **a**. $\Delta\varphi_4$ was obtained by taking the difference of two scans, one at V_{BG} = -50 V (charge neutral) and another one at V_{BG} = +50 V (electron doped). **c,** Intersubband absorption (Drude corrected $\Delta\varphi_4$) as a function of V_{BG}. The absorption increases linearly with n_{2D}, which is agreement with calculations for a perfect, infinitely deep quantum well.

increase for all N. In order to isolate the contribution due to intersubband transitions, we look at the difference in $\Delta\varphi_4$ for N = 5 and its neighbouring layers (Figure S16c). Effectively, this corresponds to a Drude correction as explained in Section V. In the Drude corrected data we observe a linear increase with V_{BG} beyond some threshold voltage of about V_{BG} = -25 V, which we attribute to the point where we start populating the conduction band with electrons. The linear increase with V_{BG} and therefore n_{2D} is in agreement with theoretical calculations for a perfect, infinitely deep quantum well.

References

1. Enkovaara, J. *et al.* Electronic structure calculations with GPAW: A real-space implementation of the projector augmented-wave method. *Journal of Physics: Condensed Matter* **22**, 253202 (2010).

2. Yeh, P. C. *et al.* Direct Measurement of the Tunable Electronic Structure of Bilayer MoS_2 by Interlayer Twist. *Nano Letters* **16**, 953–959 (2016).

3. Giannozzi, P. *et al.* QUANTUM ESPRESSO: A modular and open-source software project for quantum simulations of materials. *Journal of Physics: Condensed Matter* **21**, 395502 (2009).

4. Hicks, W. T. Semiconducting Behavior of Substituted Tungsten Diselenide and Its Analogues. *Journal of the Electrochemical Society* **111**, 1058—-1065 (1964).

5. Kormányos, A. *et al.* K·P Theory for Two-Dimensional Transition Metal Dichalcogenide Semiconductors. *2D Materials* **2**, 022001 (2015).

6. Danovich, M., Ruiz-Tijerina, D. A., Yelgel, C., Zlyomi, V. & Fal'ko, V. I. Intersubband optical transitions in multilayer transition metal dichalcogenides. *In preparation* (2018).

7. Fei, Z. *et al.* Infrared nanoscopy of dirac plasmons at the graphene-SiO_2 interface. *Nano Letters* **11**, 4701–4705 (2011).

8. Danovich, M., Aleiner, I. L., Drummond, N. D. & Falko, V. I. Fast Relaxation of Photo-Excited Carriers in 2-D Transition Metal Dichalcogenides. *IEEE Journal on Selected Topics in Quantum Electronics* **23** (2017).

9. Jin, Z., Li, X., Mullen, J. T. & Kim, K. W. Intrinsic transport properties of electrons and holes in monolayer transition-metal dichalcogenides. *Physical Review B* **90**, 045422 (2014).

10. Sohier, T., Calandra, M. & Mauri, F. Two-dimensional Fröhlich interaction in transition-metal dichalcogenide monolayers: Theoretical modeling and first-principles calculations. *Physical Review B* **94**, 085415 (2016).

11. Govyadinov, A. A. *et al.* Recovery of permittivity and depth from near-field data as a step toward infrared nanotomography. *ACS Nano* **8**, 6911–6921 (2014).

12. Bright, T., Watjen, J., Zhang, Z., Muratore, C. & Voevodin, A. Optical properties of HfO_2 thin films deposited by magnetron sputtering: From the visible to the far-infrared. *Thin Solid Films* **520**, 6793–6802 (2012).

13. Beal, A. & Liang, W. Excitons in 2H-WSe_2 and 3R-WS_2. *Journal of Physics C: Solid State Physics* **9**, 2459–2466 (1976).

14. Yun, W. S., Han, S. W., Hong, S. C., Kim, I. G. & Lee, J. D. Thickness and strain effects on electronic structures of transition metal dichalcogenides: 2H-MX_2 semiconductors (M = Mo, W; X = S, Se, Te). *Physical Review B* **85**, 033305 (2012).

15. Zhao, W. *et al.* Origin of Indirect Optical Transitions in Few-Layer MoS_2, WS_2, and WSe_2. *Nano Letters* **13**, 5627–5634 (2013).

16. Wang, Q. H., Kalantar-Zadeh, K., Kis, A., Coleman, J. N. & Strano, M. S. Electronics and optoelectronics of two-dimensional transition metal dichalcogenides. *Nature Nanotechnology* **7**, 699–712 (2012).

17. Topinka, M. A. *et al.* Imaging Coherent Electron Flow from a Quantum Point Contact. *Science* **289**, 2323–2326 (2000).

18. Topinka, M. A. *et al.* Coherent branched flow in a two-dimensional electron gas. *Nature* **410**, 183–186 (2001).